# Uniform description of breakup mechanisms in central collision, projectile fragmentation, and proton-induced spallation

Jun Su,* Long Zhu, Chenchen Guo, and Zhen Zhang
*Sino-French Institute of Nuclear Engineering and Technology, Sun Yat-sen University, Zhuhai 519082, China*

(Received 10 October 2018; revised manuscript received 6 March 2019; published 8 July 2019)

**Background:** A diversity of fragmentation modes has been observed in several types of nuclear reactions, which may correspond to different breakup mechanisms.
**Purpose:** The present work is an attempt to compare the mechanisms of the fragment emission in central heavy-ion collision near the Fermi energy, projectile fragmentation, and proton-induced spallation.
**Method:** The collisions until the prefragments with excitation energy less than 2 MeV/nucleon are studied using the isospin-dependent quantum molecular dynamics (IQMD) model, while the evaporations of light particles from the prefragments are described by the statistical code GEMINI. In the IQMD model, the binary nucleon-nucleon collisions with the Pauli blocking are applied to treat some features of fermionic motion phenomenologically. However, the binary collisions are scarce in the region where the relative momenta between the nucleons are small. Thus, the method of the phase space density constraint (PSDC) are applied in the IQMD model in order to treat phenomenologically the features of fermionic motion.
**Results:** The calculations of various observables are compared to the available data. The comparison not only shows the similar regularities of the calculations to the data, but also emphasizes the role of the PSDC method. The dynamical $E$-$\rho$ trajectories show that the compression-expansion phase in the central HIC near the Fermi energy results in the spinodal decomposition. While in the projectile fragmentation and proton-induced spallation, the projectiles are heated without compression and then cool down with slight expansion. However, driven by the dynamical fluctuations, the spinodal instability is possible for a part of the events. The perhaps most important result of this study is the significant role of the fermionic feature in the mechanisms of the fragment emission.
**Conclusions:** The IQMD + GEMINI framework provides a uniform description of breakup mechanisms in central collision, projectile fragmentation, and proton-induced spallation.

DOI: 10.1103/PhysRevC.100.014602

## I. INTRODUCTION

Phase transitions in finite systems have attracted much attention in many different fields of physics. In the case of the nuclear physics, the liquid-gas phase transition is expected to occur in the highly excited nuclei, due to the Van-der-Waals type of the nuclear force [1–3]. Over the past decades, many efforts have been devoted to explore the signals of the phase transition in the nuclear fragmentation, in which the characteristic products are the intermediate-mass fragments (IMFs) [4–6]. A large diversity of fragmentation modes has been observed in several types of nuclear reactions, including the central heavy-ion collision (HIC) near the Fermi energy, the peripheral HIC at hundreds of MeV/nucleon (also called the projectile fragmentation), and the reaction of heavy nuclei induced by nucleons or light nuclei at GeV energies (called the spallation) [7–9].

The colliding system in the central HIC near the Fermi energy undergoes successively the compression and expansion, and then decays via multifragmentation, i.e., splits into clusters and unbound nucleons in a short time span [10–13]. The theoretical explanation suggests that the spinodal decomposition is a major mechanism behind the multifragmentation phenomenon in central HIC [14,15]. Based on the spinodal scenario, the bifurcations in the dynamical trajectories, which results in the bimodal character of experimental observables, has been identified by the Boltzmann-Langevin one-body dynamics [16]. However, the interpretation as spinodal decomposition is not unique and other candidate models, such as statistical emission and binary fission, are put forward to explain the IMF production in the projectile fragmentation and proton-induced spallation [17–19].

The peripheral HIC at hundreds of MeV/nucleon is usually described by the participant-spectator model, in which the overlapping region between the projectile and target is called the participant, while the remaining parts are called the spectators [20]. The abrasion leads to the spectator at high temperature and near normal density, which will emit IMFs [21,22]. The spallation is supposed to undergo a fast nonequilibrium excitation and a slow decay process emitting products including IMFs [23,24]. Many researchers focus on the study of thermodynamic observables from the projectile fragmentation and spallation [25,26]. Others are devoted to

*Corresponding author: sujun3@mail.sysu.edu.cn

 

the dynamical analyses, such as those that suggest a similar phenomenology as spinodal instability in spallation [27]. The excitation energies both in the peripheral HIC and spallation originate from the heating but not the compression. Because of the absence of the compression-expansion phase, how the systems in those reactions access the unstable regions at low density is still an open question.

In our previous work, by showing the dynamical $E$-$\rho$ trajectories of the reactions, the onset of the multifragmentation in central HICs near the Fermi energy has been related to the spinodal instability [15]. In this work, We extend the investigation to the projectile fragmentations and the spallations, and try to clarify the possibility of the spinodal decomposition in those reactions. The uniform dynamical description of the IMF emission in the central HICs near the Fermi energy, the projectile fragmentations, and the spallations would assist us to compare the mechanisms. In another previous work, we show the isospin-dependent quantum molecular dynamics (IQMD) model, matched with the statistical description of evaporation, is able to reproduce the main features of projectile fragmentation [28]. The model will be further applied to the central HICs near the Fermi energy and the spallations.

The paper is organized as follows. In Sec. II, we describe the method. In Sec. III, we present both the results and discussions. Finally, the summaries are given in Sec. IV.

## II. THEORETICAL FRAMEWORK

One can refer to the theoretical description of the model in Ref. [28]. Here, we emphasize the method to describe for the fermionic nature in the model. The time evolution equation in the IQMD model is classical. The binary nucleon-nucleon collisions with the Pauli blocking are applied to describe the fermionic nature. However, the binary collisions are scarce in the region where the relative momenta between the nucleons are small. The centers of the projectile or target in the early stage of the reactions, and the center of the fragmenting source, are in this case. This effect has been shown in Refs. [29,30] that the momentum distribution will change from the initial the Fermi distribution to the Gaussian distribution in tens of fm/$c$.

In order to describe the fermionic nature in the region where the binary collisions are scarce, the method of the phase space density constraint (PSDC) is applied [31]. The phase space occupation probability $\overline{f}_i$ is calculated by performing the integration on a hypercube of volume $h^3$ in the phase space centered around the $i$th nucleon at each time step.

$$\overline{f}_i = 0.621 + \sum_{j\neq i}^{N} \frac{\delta_{\tau_j,\tau_i}}{2} \int_{h^3} \frac{1}{\pi^3\hbar^3} e^{-\frac{(\mathbf{r}_j-\mathbf{r}_i)^2}{2L} - \frac{(\mathbf{p}_j-\mathbf{p}_i)^2}{\hbar^2/2L}} d^3r d^3p, \tag{1}$$

where 0.621 is the contribution itself, $\tau_i$ represents isospin degree of freedom. At each time step and for each nucleon, the phase space occupation $\overline{f}_i$ is checked. If phase space occupation $\overline{f}_i$ has a value greater than 1, the momentum of the $i$th nucleon is changed randomly by many-body elastic scattering. Note that the PSDC method is a phenomenological prescription to treat some features of fermionic motion, since the full quantum mechanical description is not possible in this case.

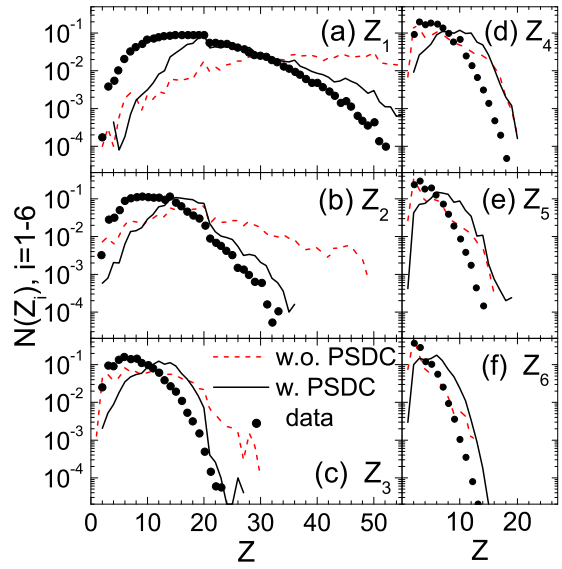


FIG. 1. Charge distribution of the six heaviest fragments in central $^{197}$Au + $^{197}$Au collisions at 35 MeV/nucleon. Experimental data, shown as points, are taken from Ref. [32]. Solid and dashed curves show the calculations by the model with and without PSDC method.

The evaporations of light particles from the prefragments are described by the statistical code GEMINI including the Hauser-Feshbach-type evaporation. By applying the GEMINI code for deexcitation of primary IQMD fragments, we assume that the density and structure of such fragments is close to the normal nuclei ones. Also we assume that properties of such fragments, in particular, the symmetry energy, level densities, and others, correspond to the properties of normal nuclei, which are adopted in the GEMINI code.

## III. RESULTS AND DISCUSSIONS

### A. Systematic comparison with experimental data

The applicability of the model in the fragmentation has been shown by comparing the calculations with ALADIN experimental data in Ref. [28]. We will continue the comparison in this section in order to emphasize the role of the PSDC method.

The experimental measurement of the multifragmentation in central $^{197}$Au + $^{197}$Au collisions at 35 MeV/nucleon has been reported in Refs. [32,33]. In the experiment, the selected central events represent about 10% of the total reaction cross section. Correspondingly, the impact parameters $b = 0$–4 fm are applied in the calculation. In order to consider the experimental filter, only the light charged particles and IMFs ($Z = 3$–20) with kinetic energy larger than $0.13Z + 1.62$ MeV/nucleon at $23^\circ \leqslant \theta_{\rm lab} \leqslant 160^\circ$, and the fragments with kinetic energy larger than 1.5 MeV/nucleon at $3^\circ \leqslant \theta_{\rm lab} \leqslant 23^\circ$ are counted in the simulation. Figure 1 shows the comparison of the charge distribution of the six heaviest fragments between the calculations and data. Because of the different geometric acceptances of the two detectors, the distributions

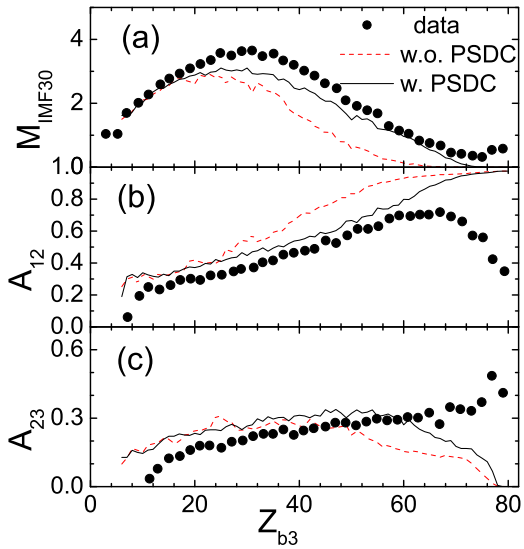


FIG. 2. Multiplicity $M_{\mathrm{IMF30}}$ of fragments with $3 \leqslant Z \leqslant 30$, the first and second fragment asymmetries $A_{12}$ and $A_{23}$ versus the analogous bound charge $Z_{b3}$ in projectile fragmentation $^{197}\mathrm{Au} + {}^{63}\mathrm{Cu}$ at 600 MeV/nucleon. Experimental data, shown as points, are taken from Ref. [34]. Solid and dashed curves show the calculations by the model with and without the PSDC method.

in Figs. 1(a) and 1(b) display a ladder at $Z = 20$. Despite the ladder, the data show that the most probable charges of the six heaviest fragments are about 20, 10, 6, 3, 3, and 2. Without the PSDC method (dashed curves), the calculations reproduce roughly the most probable charges except for the largest fragments. However, the obvious distortion occurs in the distribution of the largest fragments. The most probable charge of the largest fragments is about 50, much larger than the experimental value. In contrast, the calculations with the PSDC method (solid curves) are more consistent with the data for the largest fragments. Although the most probable charges of the calculations are larger globally than data, the down trend from the largest to sixth fragments is similar to the data. It is indicated that the model with the PSDC method reproduce the correlation between the six heaviest fragments.

For the projectile fragmentation, we will study the $^{197}\mathrm{Au} + {}^{63}\mathrm{Cu}$ collisions at 600 MeV/nucleon, the data of which has been reported in Ref. [34]. In the calculation, the projectile fragments are chosen simply by the longitudinal momentum in the center-of-mass frame. In order to consider the acceptance in the experiment, the fragments are filtered by an efficiency function $1 - 2\exp(-Z)$. Figure 2(a) shows the mean multiplicity of the IMFs as a function of the analogous bound charge $Z_{b3}$. Noting that the IMF in Ref. [34] is defined in the region $3 \leqslant Z \leqslant 30$. Thus the multiplicity of the IMFs is expressed as $M_{\mathrm{IMF30}}$. Because the threshold in the experiment is set at $Z \geqslant 3$, the analogous bound charge $Z_{b3}$ is defined as the sum over all fragments with $Z \geqslant 3$. It has been proved that the analogous bound charge $Z_{b3}$ is equivalent to the well-known bound charge when describing the violence of the collision. Both the calculations with and without the PSDC method reproduce the rise and fall of the data. However, without the PSDC method, the model substantially underestimates the multiplicity of the IMFs at the large $Z_{b3}$ region, i.e., for the peripheral collision. Figures 2(b) shows the charge asymmetry $A_{12}$ between the two largest fragments, while Fig. 2(c) for the charge asymmetry $A_{23}$ between the second and third largest fragments. The value $A_{12} = 0$ means the same charges of the two largest fragments, while the value close to 1 means nucleon evaporation. The data shows the increase of $A_{12}$ with increasing $Z_{b3}$, but reaches the maximum near $Z_{b3} = 68$. The decrease of $A_{12}$ for $Z_{b3} > 68$ may be caused by the fragments from the target. The value $Z_{b3} = 79$ correspond to the collision at large impact parameter, in which the excitation energy is very low and several neutrons evaporate from the projectile Au. In this case, $A_{12}$ should be close to 1, but not 0.3 as shown in the data. For the same reason, the charge asymmetry $A_{23}$ between the second and third largest fragment for $Z_{b3} = 79$ should be 0, but not 0.4 as shown in the data. Both calculations with and without the PSDC method show the monotonously increase of $A_{12}$ with increasing $Z_{b3}$, neglecting the statistical errors. However, the PSDC method makes the calculation more consistent with the data. In the $A_{23}$ case, the PSDC method change values near $Z_{b3}$. But one can not conclude the advantage of the PSDC method by comparing to the data of $A_{23}$.

In another experimental work [35,36], which manages the projectile fragmentation in $^{197}\mathrm{Au} + {}^{12}\mathrm{C}$ collisions at 1000 MeV/nucleon, the violence of the collision was described by the multiplicity of charged fragments $m_C$. The fluctuations in the size of the largest fragment $\Delta_{Amax}$, and the reduced variance $\gamma_2$ are applied to identify the critical point, which is expressed as the $m_C$ value. The reduced variance $\gamma_2$ is related to the moments analysis. The $k$ moments $M_k$ of the cluster size distribution given by,

$$M_k(m_C) = \Sigma A^k n_A(m_C); \quad k = 0, 1, 2, \text{and } 3, \tag{2}$$

where $n_A$ is the number of the fragments with mass number $A$, the sum runs over all masses in the event including neutrons except for the heaviest fragment. Then reduced variance $\gamma_2$ is defined as the combination of moments,

$$\gamma_2 = M_2 M_0 / M_1^2. \tag{3}$$

Being similar to the multiplicity of IMFs $M_{\mathrm{IMF30}}$, both the $\Delta_{Amax}$ and $\gamma_2$ display the rise and fall with increasing $m_C$, as shown in Figs. 3(a), 3(b), and 3(c). The data of $\Delta_{Amax}$ and $\gamma_2$ indicate the critical point near $m_C = 28$. But the peak in $M_{\mathrm{IMF30}}$ is not as well defined as for the critical point. Regarding the calculations, the model without the PSDC method underestimates the production of the IMFs, and suggests the critical point near $m_C = 42$. In contrast, the predictions of the model with the PSDC method is better. The PSDC method not only enhances the production of the IMFs, but also reduces the critical point to $m_C = 32$, which is near to the experimental one. However, from Fig. 3(d), one can not see the advantage of the PSDC method when describe the correlation between the third and second moments.

Let us turn to the spallation in $^{56}\mathrm{Fe} + p$ collisions at 1000 MeV/nucleon, for which the data are advisable in Ref. [17]. In the experiment, the energy threshold at center-of-mass frame is very low, while the detection efficiency is 78% for He, 83% for Li, and >94% for heavier fragments. In the

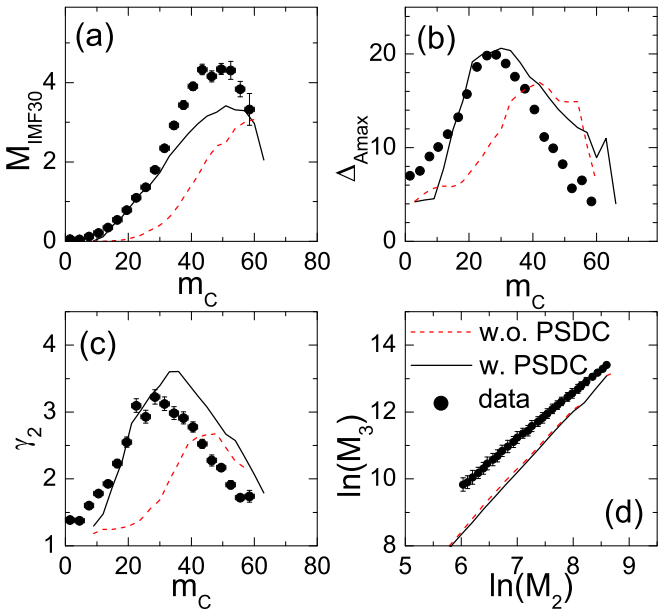


FIG. 3. (a) Multiplicity of fragments with $3 \leqslant Z \leqslant 30$ $M_{\mathrm{IMF30}}$ versus multiplicity of charged fragments $m_C$, (b) Fluctuations in the size of the largest fragment $\Delta_{Amax}$ versus $m_C$, (c) reduced variance $\gamma_2$ versus $m_C$, and (d) correlation between the third and second moments, i.e., $\ln(M_3)$ vs. $\ln(M_2)$, in projectile fragmentation $^{197}$Au + $^{12}$C at 1000 MeV/nucleon. The definitions of the reduced variance $\gamma_2$, second moment $M_2$, and third moment $M_3$ are given in the text. Experimental data, shown as points, are taken from Refs. [35,36]. Solid and dashed curves show the calculations by the model with and without the PSDC method.

calculations, the filter is not applied. Figure 4 shows the mean multiplicities per event as a function of the total bound charge $Z_{\mathrm{bound}}$ for the fragments with $Z = 2$–7. It is shown that all multiplicities increase as the collision becomes more violent, i.e., decreasing $Z_{\mathrm{bound}}$. The yields of the IMFs are so low even for the most violent collision, only in the order of 0.1 for each element. This phenomenon has been considered as one of the elusive evidences for multifragmentation in the spallation [19]. It has been shown that the GEMINI model including the Hauser-Feshbach-type evaporation and binary splitting can reproduce the data [17]. In our calculations, only the evaporation channel is allowed in the GEMINI code. By describing the productions of the IMFs dynamically, our model with the PSDC method also reproduces the data. Furthermore, the PSDC method plays a key role in enhancing the yields of the IMFs in the model. The suggested dynamical description may be considered as an alternative to the statistical description of the fragment formation in these reactions [37], which was used in the mentioned experimental papers.

### B. Breakup mechanisms in different fragmentation modes

As shown in the preceding section, our model can uniformly describe the fragmentations in central collision, projectile fragmentation, and spallation. In this section, we will compare the breakup mechanisms in those three types of fragmentations. We chose the incident energy and impact parameters so that the masses and excitation energies of the fragmenting sources produced in those three types of reactions are similar. As shown in Table I, the central ($b = 0$ fm) $^{48}$Ti + $^{48}$Ti collision at 30 MeV/nucleon, $^{120}$Sn + $^{120}$Sn collision at 600 MeV/nucleon with impact parameter $b = 8$ fm, and $^{90}$Zr + $p$ collision at 2000 MeV/nucleon with $b = 0$ fm are chosen. Figure 5 shows the correlations between the mass and the excitation energy of the equilibrated fragmenting sources in those collisions. The equilibrated fragmenting sources are distinguished by the minimum spanning tree algorithm together with the ratio of parallel to transverse quantities [28]. It is shown that

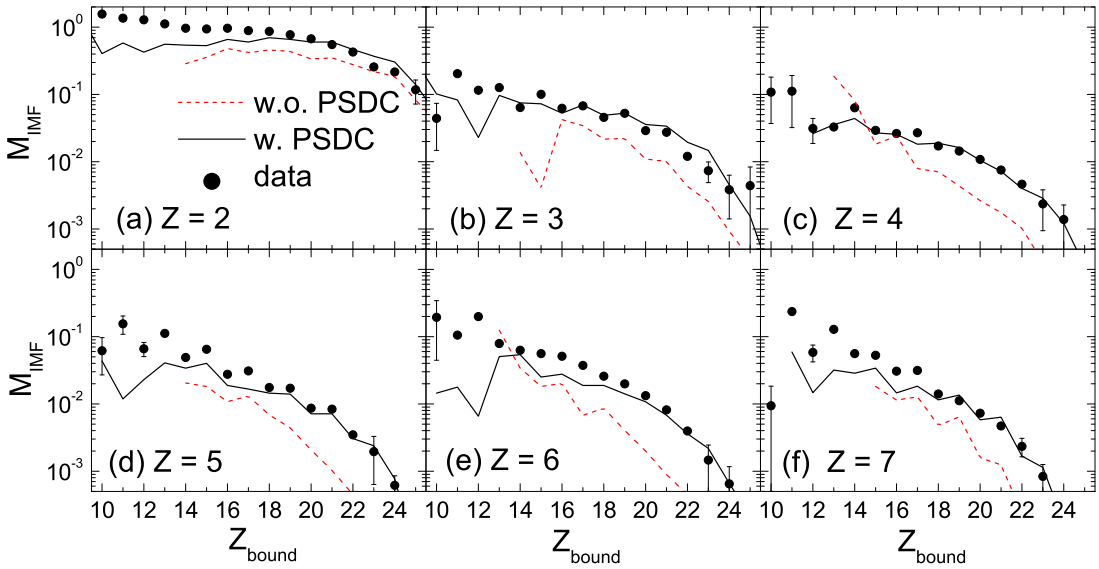


FIG. 4. Mean multiplicities per event as a function of the total bound charge $Z_{\mathrm{bound}}$ for the fragments with $Z = 2$–7 produced in $^{56}$Fe + $p$ collisions at 1000 MeV/nucleon. Experimental data, shown as points, are taken from Refs. [17]. Solid and dashed curves show the calculations by the model with and without the PSDC method.

TABLE I. Central HIC near the Fermi energy, projectile fragmentation, and proton-induced spallation studied in this work.

| | Cent. coll. | Proj. frag. | $p$ spallation |
|---|---|---|---|
| System | $^{48}$Ti + $^{48}$Ti | $^{120}$Sn + $^{120}$Sn | $^{90}$Zr + $p$ |
| $E$ (MeV/nucl.) | 30 | 600 | 2000 |
| $b$ (fm) | 0 | 8 | 0 |

all collisions produce the fragmenting sources with mass number near 90 and excitation energy near 7 MeV/nucleon. In the central collision at 30 MeV/nucleon, the fragmenting source is formed by the incomplete fusion between two $^{48}$Ti nuclei. The narrow $A$-$E^*$ distribution around the system mass (96) and the available energy (7.5 MeV/nucleon) indicate that only few nucleons are emitted during the incomplete fusion. In the peripheral collision of $^{120}$Sn + $^{120}$Sn at 600 MeV/nucleon, the strong dissipation between the projectile and target causes the large fluctuations. Hence the wide $A$-$E^*$ distribution of the fragmenting source is observed. In the proton-induced spallation at 2000 MeV/nucleon, only less than half the available energy (21.74 MeV/nucleon) dissipates in the fragmenting source. The excitation energy extends over a wide region, from 0–10 MeV/nucleon.

Within the local density approximation, one may consider the central area of the colliding system as a thermodynamic subsystem in a grand canonical ensemble. In order to show the time evolutions of the thermodynamic properties, the energies per nucleon $E$ of the projectile centers (1 fm$^3$ sphere) during the collisions are calculated from the density $\rho$ and the transverse kinetic energy $E_{tr}$.

$$E = \frac{\alpha}{2}\frac{\rho}{\rho_0} + \frac{\beta}{\gamma+1}\left(\frac{\rho}{\rho_0}\right)^{\gamma} + \frac{3}{2}\overline{E_{tr}}. \quad (4)$$

The symmetry energy is not considered since it is insignificant for the mechanism of the fragmentation [15]. The transverse kinetic energy is used to deduct the translational energy from the total energy.

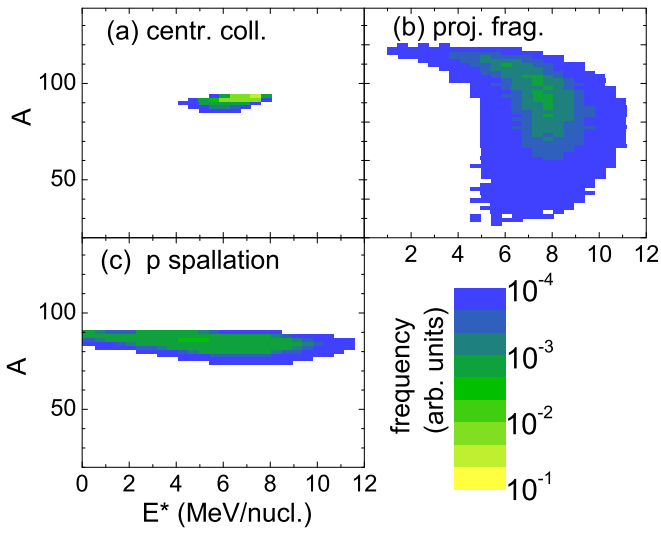


FIG. 5. Correlations between mass and the excitation energy of the equilibrated fragmenting sources in the central collision, projectile fragmentation, and proton-induced spallation.

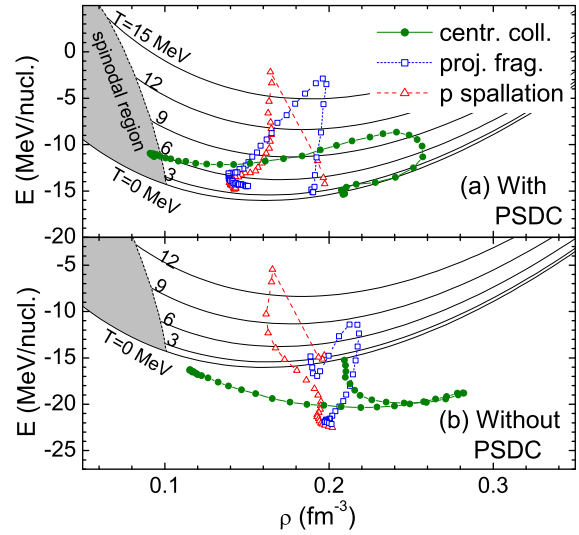


FIG. 6. Dynamical $E$-$\rho$ trajectories of the projectile centers (1 fm$^3$ sphere) in the central $^{48}$Ti + $^{48}$Ti collision at 30 MeV/nucleon, $^{120}$Sn + $^{120}$Sn collision at 600 MeV/nucleon with $b = 8$ fm, and $^{90}$Zr + $p$ collision at 2000 MeV/nucleon with $b = 0$ fm, calculated by the IQMD model (a) with PSDC improvement and (b) without PSDC improvement. The solid curves show the energy per nucleon versus density of the nuclear matter at finite temperature. The grays show the spinodal region, in which the isothermal compressibility has a negative value.

Figure 6(a) shows the dynamical $E$-$\rho$ trajectories of the projectile centers in the pertinent collisions, calculated with the IQMD model using the PSDC method. The time separation of the plotted points is 2 fm/$c$. The energies per nucleon versus density at different temperatures and the spinodal region for the nuclear matter are also plotted in the figure. For the central $^{48}$Ti + $^{48}$Ti collision at 30 MeV/nucleon, the $E$-$\rho$ trajectory shows a half cycle with a tail. This corresponds to the compression and heating at the beginning of the collision, and then the expansion and cooling by the light particle emission. The maximum density is 0.25 fm$^{-3}$, and the maximum temperature is 10 MeV. This means that the incident energies dissipate into both potential energies and kinetic energies. The ending of the $E$-$\rho$ trajectory is in the spinodal region, indicating the instability of the system. The dynamical trajectory for the peripheral collision of $^{120}$Sn + $^{120}$Sn at 600 MeV/nucleon shows that the center of the projectile is heated with hardly any compression. In 20 fm/$c$, the temperature increases to 17 MeV, but the increment of the density is only 0.01 fm$^{-3}$. The cooling stage is accompanied with the expansion. However, before the trajectory reaches the spinodal region, the density transforms to increase slightly. In the case of the spallation, the $^{90}$Zr nucleus is heated by the proton. The hot nucleons diffuse outward, causing the decrease of the density. The ending point of the $E$-$\rho$ trajectory is also far from the spinodal region.

In order to study the effects of the PSDC improvement, we show the dynamical $E$-$\rho$ trajectory without PSDC

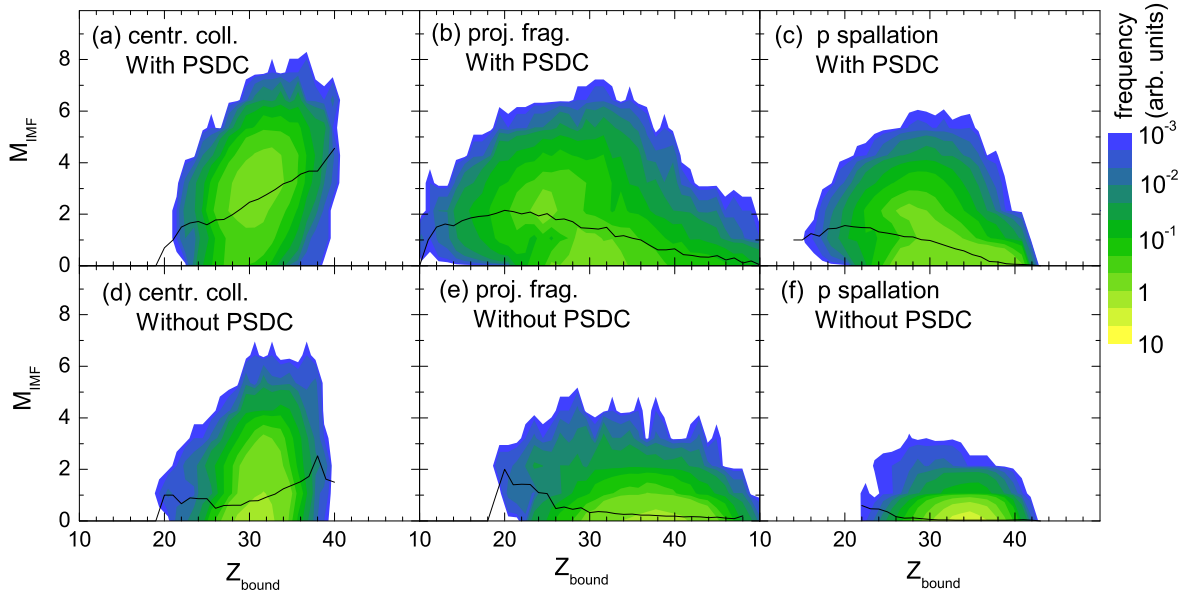


FIG. 7. Correlations between the multiplicity of IMFs and the total bound charge $Z_{\text{bound}}$ of the productions in the central collision, projectile fragmentation, and proton-induced spallation calculated by the IQMD + GEMINI model with and without PSDC improvement. The solid curves show the mean multiplicity of IMFs as a function of $Z_{\text{bound}}$.

improvement in Fig. 6(b). The role of the PSDC method in the model is to treat the features of fermionic motion, and avoid the transformation of the momentum distribution from the initial Fermi type to the Gaussian type. The transformation of the momentum distribution causes the decrease of the thermal energy and increase of the density in the center of the nucleus. Both in Figs. 6(a) and 6(b), the compression and heating in the central collision, as well as the heating in the projectile fragmentation and spallation can be observed. However, the $E$-$\rho$ trajectories of the projectile center in Fig. 6(b) evolve to the region of the negative temperature. Concurrently, the densities evolve to the high-density region, which is far from the spinodal region. The $E$-$\rho$ curves at different temperatures of the nuclear matter are calculated based on the Fermi distribution. The negative temperature indicates the deviation from Fermi distribution for the colliding system.

The effects of the PSDC improvement can be also observed by studying the precursors of the IMFs. Campi *et al.* proposed a scenario in which the power-law fragment distribution is already produced at the high-density phase of the reaction, and then preserved during expansion [38]. We examine this scenario by simulating the evolution of $^{90}$Zr. The minimum spanning tree algorithm (see Ref. [28]) with $R_0 = 2$ fm and $P_0 = 200$ MeV/$c$ is applied to distinguish the clusters. The abundant clusters are found in the initial state and preserved during the evolution when PSDC method is applied. But when PSDC method is not considered, some of the initial clusters assemble and become large clusters, while others disperse to light clusters and nucleons during the evolution. That is to say, the PSDC improvement helps to preserve the precursors of the IMFs, which may cease to interact with each other and become the observable fragments when the average density of the system decrease.

In Ref. [15], it has been shown that the dynamics trajectory in the central HICs will reach the spinodal region only for incident energy larger than 25 MeV/nucleon. This energy corresponds to the threshold of the multifragmentation in central HICs, indicating the relation between the IMF emission and spinodal mechanism. Figure 6 shows that only the dynamics trajectory in the central HICs will reach the spinodal region, although excitation energy of the hot systems formed in the three types of reaction are similar. Thus, it is necessary to compare the yields of the IMFs in the three types of reactions. The correlations between the multiplicity of IMFs and the total bound charge $Z_{\text{bound}}$ of the productions are calculated with the IQMD + GEMINI model. Figures 7(a)–7(c) show the results with the PSDC improvement. In the case of the central $^{48}$Ti + $^{48}$Ti collision [Fig. 7(a)], the mean $M_{\text{IMF}}$ increases monotonously with $Z_{\text{bound}}$. The most probable value of $M_{\text{IMF}}$ is about 3, and that of $Z_{\text{bound}}$ is 30. This means that the multifragmentation, rather than the evaporation, is dominated in the decay process. As mentioned above, the dynamical $E$-$\rho$ trajectory of the projectile center reaches the spinodal region, where the compressibility is negative. A homogeneous medium will fragment when it reaches the spinodal region. We can argue this scenario in the case of the infinite nuclear matter. But we may have another scenario in the case of the finite system in the HICs. In fact, the dynamical $E$-$\rho$ trajectory shown above is the ensemble average, which is calculated using 100 000 events. When the ensemble average of the compressibility is negative, a large fraction of the phase space is populated for each event. Thus, the phase spaces with IMFs are available.

The ensemble average of the energy and density do not show the spinodal character for the projectile fragmentation and spallation. But those reactions also produce the IMFs [see Figs. 7(b) and 7(c)]. In the case of the projectile fragmentation, the mean $M_{\text{IMF}}$ rises and then falls with increasing $Z_{\text{bound}}$. Furthermore, two most disconnected regions of the $M_{\text{IMF}}$ vs $Z_{\text{bound}}$ correlations are observed. One is near the region with

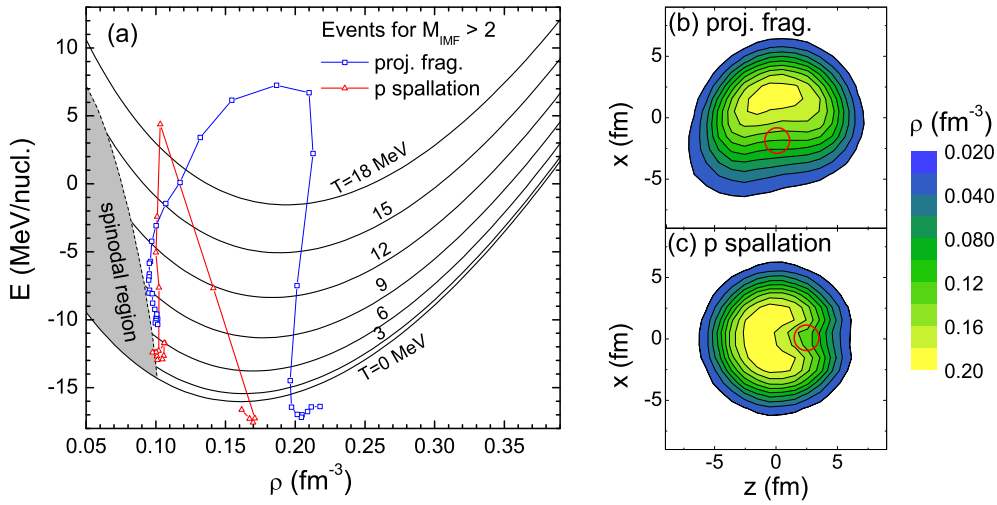


FIG. 8. (a) Dynamical $E$-$\rho$ trajectory of the fragmenting area in the $^{120}$Sn + $^{120}$Sn collision at 600 MeV/nucleon with $b = 8$ fm and $^{90}$Zr + $p$ collision at 2000 MeV/nucleon with b = 0 fm. In the calculations, only the events with $M_{\rm IMF} > 2$ are considered. (b) Density distribution of the fragmenting source in the $^{120}$Sn + $^{120}$Sn collision. (c) Density distribution of the fragmenting source in the $^{90}$Zr + $p$ collision. The circles (in red online) show the fragmenting area.

$M_{\rm IMF} = 2.5$ and $Z_{\rm bound} = 25$, and the other is close to the axis of $M_{\rm IMF} = 0$. This type of bimodal character has been observed by studying the experimental observables, such as the size of the heaviest cluster [39], and the asymmetry between the charges of the two heaviest clusters [40]. Two more regions can be also identified in the case of the spallation, although they are very close to each other. It has been argued that the bimodality is related to the dynamical bifurcations at the boundary of the phase separation [16].

Concerning the calculations without PSDC improvement [Figs. 7(d)–7(f)], the mean $M_{\rm IMF}$ in all cases are smaller than the corresponding values with PSDC improvement. Furthermore, the most probable $M_{\rm IMF}$-$Z_{\rm bound}$ correlations in all cases move to the region near the axis of $M_{\rm IMF} = 0$, indicating the dominance of the nucleon evaporation, rather than the fragmentation. It is indicated that the fermionic feature, which is treated phenomenologically by the PSDC improvement, plays an important role in the fragment emission, not only in central HICs near the Fermi energy but also in the projectile fragmentation and spallation.

In order to probe the mechanisms of the IMF emission in the projectile fragmentation and the proton-induced spallation, we investigate the $E$-$\rho$ evolutions not only of the projectile center but also of other subsystems in the fragmenting source. It is found that, both in the cases of the projectile fragmentation and spallation, there are areas where the $E$-$\rho$ trajectories reach the spinodal region, as shown in Fig. 8. Let us call those areas fragmenting areas. Figure 8(a) displays the dynamical $E$-$\rho$ trajectories. In the calculations, only the events with $M_{\rm IMF} > 2$ are considered. Figures 8(b) and 8(c) interpret the location of the fragmenting area. The fragmenting area in the case of the projectile fragmentation is in the spectator but close to the participant. This area is heated by the hyperthermal participant. Some of the nucleons escape from the nonequilibrium spectator, resulting in the decrease of the density. Analogously, the fragmenting area in the case of the spallation is heated by the high-speed proton, causing the decrease of the density. Since the $E$-$\rho$ trajectories of the fragmenting areas reach the spinodal region, the clusters and unbound nucleons would be produced through the spinodal decomposition mechanism. It is indicated that the mechanisms of the IMF emission in the projectile fragmentation and spallation is similar to that in dissipative central heavy-ion collisions near the Fermi energy. We have demonstrated the sensitivity of $E$-$\rho$ trajectories to the detail of the dynamical treatment. However, the fragment formation is additionally regulated by the finite-size effects, which should be considered also.

## IV. CONCLUSION

In summary, the calculations of various observables by the IQMD + GEMINI model are compared to the available data. The calculations demonstrate similar regularities of fragment production as in experimental data. Moreover, it emphasizes the role of the PSDC method. Then we devote ourself to comparing the mechanisms of the fragment emission in the central ($b = 0$ fm) $^{48}$Ti + $^{48}$Ti collision at 30 MeV/nucleon, $^{120}$Sn + $^{120}$Sn collision at 600 MeV/nucleon with impact parameter $b = 8$ fm, and $^{90}$Zr + $p$ collision at 2000 MeV/nucleon with $b = 0$ fm. These collisions produce fragmenting sources with similar mass ($A \approx 90$) and excitation energies ($E^* \approx 7$ MeV/nucleon). The dynamical $E$-$\rho$ trajectories show that the hot and compressed nuclear system formed in the central $^{48}$Ti + $^{48}$Ti expands and cools to the spinodal region, and then splits in a short time span due to the instability. This mechanism results in the abundant production of intermediate-mass fragments. The incident energies in the projectile fragmentation and spallation mainly dissipate into thermal energies. The projectiles are heated without compression and then cool down with slight expansion. The dynamical $E$-$\rho$ trajectories calculated using all events are far from the spinodal region. However, driven by the dynamical fluctuations, the spinodal instability is possible

for a part of the events. Some nucleons escape from the nonequilibrium system, causing the decrease of the density and thereby bringing the system into the spinodal region. Note that this is just a theoretical assumption, with promise to study more a realistic phase diagram in the future.

The perhaps most important result of this study is the significant role of the fermionic feature in the mechanisms of the fragment emission. The method of the phase space density constraint (PSDC) is applied to treat phenomenologically some features of fermionic motion, since the full quantum mechanical description is not possible in the isospin-dependent quantum molecular dynamics model. The application of the PSDC method avoids the evolution of the momentum distribution from the initial Fermi-Dirac type to the Gaussian type, and hence eliminates the overbinding (larger density and smaller kinetic energy) in the center of the nucleus. The latter suppresses the fragment emission and enhances the nucleon evaporation. The comparison between the calculations with and without the PSDC method suggests that missing the fermionic feature in the transport model is responsible for the observed underestimation of the fragment yields in the projectile fragmentation [41].

## ACKNOWLEDGMENTS

This work was supported by the National Natural Science Foundation of China under Grants No. 11875328, No. 11605296, and No. 11605270, and the Natural Science Foundation of Guangdong Province China under Grant No. 2016A030310208. The authors are grateful to W. Trautmann for helpful and detailed discussions.

[1] K. Binder and D. P. Landau, Phys. Rev. B **30**, 1477 (1984).
[2] A. Guarnera, M. Colonna, and P. Chomaz, Phys. Lett. B **373**, 267 (1996).
[3] P. Chomaz, V. Duflot, and F. Gulminelli, Phys. Rev. Lett. **85**, 3587 (2000).
[4] C.-Y. Wong and K. VanBibber, Phys. Rev. C **25**, 2990 (1982).
[5] W. Trautmann, P. Adrich, T. Aumann, C. O. Bacri, T. Barczyk, R. Bassini, S. Bianchin, C. Boiano, A. S. Botvina, A. Boudard, J. Brzychczyk, A. Chbihi, J. Cibor, B. Czech, M. de Napoli, J. é. Ducret, H. Emling, J. D. Frankland, M. Hellström, D. Henzlova, G. Immè, I. Iori, H. Johansson, K. Kezzar, A. Lafriakh, A. L. fèvre, E. L. Gentil, Y. Leifels, J. Lühning, J. łukasik, W. G. Lynch, U. Lynen, Z. Majka, M. Mocko, W. F. J. Müller, A. Mykulyak, H. Orth, A. N. Otte, R. Palit, P. Pawłowski, A. Pullia, G. Raciti, E. Rapisarda, H. Sann, C. Schwarz, C. Sfienti, H. Simon, K. Sümmerer, M. B. Tsang, G. Verde, C. Volant, M. Wallace, H. Weick, J. Wiechula, A. Wieloch, and B. Zwiegliński, Int. J. Mod. Phys. E **17**, 1838 (2008).
[6] B. Borderie and M. Rivet, Prog. Part. Nucl. Phys. **61**, 551 (2008).
[7] J. Pochodzalla, T. Möhlenkamp, T. Rubehn, A. Schüttauf, A. Wörner, E. Zude, M. Begemann-Blaich, Th. Blaich, H. Emling, A. Ferrero, C. Gross, G. Immé, I. Iori, G. J. Kunde, W. D. Kunze, V. Lindenstruth, U. Lynen, A. Moroni, W. F. J. Müller, B. Ocker, G. Raciti, H. Sann, C. Schwarz, W. Seidel, V. Serfling, J. Stroth, W. Trautmann, A. Trzcinski, A. Tucholski, G. Verde, and B. Zwieglinski, Phys. Rev. Lett. **75**, 1040 (1995).
[8] S. Hudan, A. Chbihi, J. D. Frankland, A. Mignon, J. P. Wieleczko, G. Auger, N. Bellaize, B. Borderie, A. Botvina, R. Bougault, B. Bouriquet, A. M. Buta, J. Colin, D. Cussol, R. Dayras, D. Durand, E. Galichet, D. Guinet, B. Guiot, G. Lanzalone, P. Lautesse, F. Lavaud, J. F. Lecolley, R. Legrain, N. Le Neindre, O. Lopez, L. Manduci, J. Marie, L. Nalpas, J. Normand, M. Pârlog, P. Pawłowski, M. Pichon, E. Plagnol, M. F. Rivet, E. Rosato, R. Roy, J. C. Steckmeyer, G. Tăbăcaru, B. Tamain, A. van Lauwe, E. Vient, M. Vigilante, and C. Volant (INDRA Collaboration), Phys. Rev. C **67**, 064613 (2003).
[9] P. Napolitani, K.-H. Schmidt, A. S. Botvina, F. Rejmund, L. Tassan-Got, and C. Villagrasa, Phys. Rev. C **70**, 054607 (2004).
[10] C. Ngô, Nucl. Phys. A **488**, 233 (1988).
[11] P. Lautesse, A. M. Maskay, E. Gerlic, P. Désesquelles, J. L. Laville, O. Lopez, B. Borderie, R. Dayras, A. Demeyer, D. Durand, J. D. Frankland, E. Galichet, D. Guinet, B. Guiot, N. Le Neindre, J. Marie, L. Nalpas, M. Pârlog, M. Pichon, M. F. Rivet, E. Rosato, R. Roy, C. Schmitt, B. Tamain, E. Vient, M. Vigilante, C. Volant, and J. P. Wieleczko (INDRA Collaboration), Phys. Rev. C **71**, 034602 (2005).
[12] L. Shvedov, M. Colonna, and M. DiToro, Phys. Rev. C **81**, 054605 (2010).
[13] G. Ademard, J. P. Wieleczko, J. Gomez del Campo, M. La Commara, E. Bonnet, M. Vigilante, A. Chbihi, J. D. Frankland, E. Rosato, G. Spadaccini, Sh. A. Kalandarov, C. Beck, S. Barlini, B. Borderie, R. Bougault, R. Dayras, G. De Angelis, J. De Sanctis, V. L. Kravchuk, P. Lautesse, N. Le Neindre, J. Moisan, A. D'Onofrio, M. Parlog, D. Pierroutsakou, M. F. Rivet, M. Romoli, R. Roy, G. G. Adamian, and N. V. Antonenko, Phys. Rev. C **83**, 054619 (2011).
[14] P. Chomaz, M. Colonna, and J. Randrup, Phys. Rep. **389**, 263 (2004).
[15] J. Su, L. Zhu, and C. Guo, Phys. Lett. B **782**, 682 (2018).
[16] P. Napolitani and M. Colonna, Phys. Lett. B **726**, 382 (2013).
[17] E. Le Gentil, T. Aumann, C. O. Bacri, J. Benlliure, S. Bianchin, M. Böhmer, A. Boudard, J. Brzychczyk, E. Casarejos, M. Combet, L. Donadille, J. E. Ducret, M. Fernandez-Ordoñez, R. Gernhäuser, H. Johansson, K. Kezzar, T. Kurtukian-Nieto, A. Lafriakh, F. Lavaud, A. Le Fèvre, S. Leray, J. Lühning, J. Lukasik, U. Lynen, W. F. J. Müller, P. Pawlowski, S. Pietri, F. Rejmund, C. Schwarz, C. Sfienti, H. Simon, W. Trautmann, C. Volant, and O. Yordanov, Phys. Rev. Lett. **100**, 022701 (2008).
[18] R. Ogul, A. S. Botvina, U. Atav, N. Buyukcizmeci, I. N. Mishustin, P. Adrich, T. Aumann, C. O. Bacri, T. Barczyk, R. Bassini, S. Bianchin, C. Boiano, A. Boudard, J. Brzychczyk, A. Chbihi, J. Cibor, B. Czech, M. D. Napoli, J.-É. Ducret, H. Emling, J. D. Frankland, M. Hellström, D. Henzlova, G. Immè, I. Iori, H. Johansson, K. Kezzar, A. Lafriakh, A. L. Fèvre, E. L. Gentil, Y. Leifels, J. Lühning, J. Łukasik, W. G. Lynch, U. Lynen, Z. Majka, M. Mocko, W. F. J. Müller, A. Mykulyak, H. Orth, A. N. Otte, R. Palit, P. Pawłowski, A. Pullia, G. Raciti, E. Rapisarda, H. Sann, C. Schwarz, C. Sfienti, H. Simon, K. Sümmerer, W. Trautmann, M. B. Tsang, G. Verde,

C. Volant, M. Wallace, H. Weick, J. Wiechula, A. Wieloch, and B. Zwiegliński, Phys. Rev. C **83**, 024608 (2011).
[19] D. Mancusi, A. Boudard, J. Cugnon, J.-C. David, T. Gorbinet, and S. Leray, Phys. Rev. C **84**, 064615 (2011).
[20] B. K. Singh and S. K. Tuli, Il Nuovo Cimento A **112**, 1093 (1999).
[21] D. Pérez-Loureiro, J. Benlliure, H. Álvarez-Pol, B. Blank, E. Casarejos, D. Dragosavac, V. Föhr, M. Gascón, W. Gawlikowicz, A. Heinz, K. Helariutta, A. Kelić-Heil, S. Lukić, F. Montes, L. Pieńkowski, K.-H. Schmidt, M. Staniou, K. Subotić, K. Sümmerer, J. Taieb, and A. Trzcińska, Phys. Lett. B **703**, 552 (2011).
[22] S. D. Gupta, S. Mallik, and G. Chaudhuri, Phys. Lett. B **726**, 427 (2013).
[23] R. Serber, Phys. Rev. **72**, 1114 (1947).
[24] J. Hüfner, Phys. Rep. **125**, 129 (1985).
[25] A. Kelić, J. B. Natowitz, and K. H. Schmidt, Eur. Phys. J. A **30**, 203 (2006).
[26] V. Viola, K. Kwiatkowski, L. Beaulieu, D. Bracken, H. Breuer, J. Brzychczyk, R. de Souza, D. Ginger, W.-C. Hsi, R. Korteling, T. Lefort, W. Lynch, K. Morley, R. Legrain, L. Pienkowski, E. Pollacco, E. Renshaw, A. Ruangma, M. Tsang, C. Volant, G. Wang, S. Yennello, and N. Yoder, Phys. Rep. **434**, 1 (2006).
[27] P. Napolitani and M. Colonna, Phys. Rev. C **92**, 034607 (2015).
[28] J. Su, W. Trautmann, L. Zhu, W.-J. Xie, and F.-S. Zhang, Phys. Rev. C **98**, 014610 (2018).
[29] J. Xu, L.-W. Chen, ManYee B. Tsang, H. Wolter, Y.-X. Zhang, J. Aichelin, M. Colonna, D. Cozma, P. Danielewicz, Z.-Q. Feng, A. L. Fèvre, T. Gaitanos, C. Hartnack, K. Kim, Y. Kim, C.-M. Ko, B.-A. Li, Q.-F. Li, Z.-X. Li, P. Napolitani, A. Ono, M. Papa, T. Song, J. Su, J.-L. Tian, N. Wang, Y.-J. Wang, J. Weil, W.-J. Xie, F.-S. Zhang, and G.-Q. Zhang, Phys. Rev. C **93**, 044609 (2016).
[30] Y.-X. Zhang, Y.-J. Wang, M. Colonna, P. Danielewicz, A. Ono, M. B. Tsang, H. Wolter, J. Xu, L.-W. Chen, D. Cozma, Z.-Q. Feng, S. D. Gupta, N. Ikeno1, C.-M. Ko, B.-A. Li, Q.-F. Li, Z.-X. Li, S. Mallik, Y. Nara, T. Ogawa, A. Ohnishi, D. Oliinychenko, M. Papa, H. Petersen, J. Su, T. Song, J. Weil, N. Wang, F.-S. Zhang, and Z. Zhang, Phys. Rev. C **97**, 034625 (2018).
[31] M. Papa, T. Maruyama, and A. Bonasera, Phys. Rev. C **64**, 024612 (2001).
[32] M. D'Agostino, A. Botvina, P. Milazzo, M. Bruno, G. Kunde, D. Bowman, L. Celano, N. Colonna, J. Dinius, A. Ferrero, M. Fiandri, C. Gelbke, T. Glasmacher, F. Gramegna, D. Handzy, D. Horn, W. Hsi, M. Huang, I. Iori, M. Lisa, W. Lynch, L. Manduci, G. Margagliotti, P. Mastinu, I. Mishustin, C. Montoya, A. Moroni, G. Peaslee, F. Petruzzelli, L. Phair, R. Rui, C. Schwarz, M. Tsang, G. Vannini, and C. Williams, Phys. Lett. B **371**, 175 (1996).
[33] M. D'Agostino, G. J. Kunde, P. M. Milazzo, J. D. Dinius, M. Bruno, N. Colonna, M. L. Fiandri, C. K. Gelbke, T. Glasmacher, F. Gramegna, D. O. Handzy, W. C. Hsi, M. Huang, M. A. Lisa, W. G. Lynch, P. F. Mastinu, C. P. Montoya, A. Moroni, G. F. Peaslee, L. Phair, R. Rui, C. Schwarz, M. B. Tsang, G. Vannini, and C. Williams, Phys. Rev. Lett. **75**, 4373 (1995).
[34] A. Botvina, I. Mishustin, M. Begemann-Blaich, J. Hubele, G. Imme, I. Iori, P. Kreutz, G. Kunde, W. Kunze, V. Lindenstruth, U. Lynen, A. Moroni, W. Müller, C. Ogilvie, J. Pochodzalla, G. Raciti, T. Rubehn, H. Sann, A. Schüttauf, W. Seidel, W. Trautmann, and A. Wörner, Nucl. Phys. A **584**, 737 (1995).
[35] B. K. Srivastava, S. Albergo, F. Bieser, F. P. Brady, Z. Caccia, D. A. Cebra, A. D. Chacon, J. L. Chance, Y. Choi, S. Costa, J. B. Elliott, M. L. Gilkes, J. A. Hauger, A. S. Hirsch, E. L. Hjort, A. Insolia, M. Justice, D. Keane, J. C. Kintner, V. Lindenstruth, M. A. Lisa, H. S. Matis, M. McMahan, C. McParland, W. F. J. Müller, D. L. Olson, M. D. Partlan, N. T. Porile, R. Potenza, G. Rai, J. Rasmussen, H. G. Ritter, J. Romanski, J. L. Romero, G. V. Russo, H. Sann, R. P. Scharenberg, A. Scott, Y. Shao, T. J. M. Symons, M. Tincknell, C. Tuvé, S. Wang, P. Warren, H. H. Wieman, T. Wienold, and K. Wolf (EOS Collaboration), Phys. Rev. C **64**, 041605(R) (2001).
[36] R. P. Scharenberg, B. K. Srivastava, S. Albergo, F. Bieser, F. P. Brady, Z. Caccia, D. A. Cebra, A. D. Chacon, J. L. Chance, Y. Choi, S. Costa, J. B. Elliott, M. L. Gilkes, J. A. Hauger, A. S. Hirsch, E. L. Hjort, A. Insolia, M. Justice, D. Keane, J. C. Kintner, V. Lindenstruth, M. A. Lisa, H. S. Matis, M. McMahan, C. McParland, W. F. J. Müller, D. L. Olson, M. D. Partlan, N. T. Porile, R. Potenza, G. Rai, J. Rasmussen, H. G. Ritter, J. Romanski, J. L. Romero, G. V. Russo, H. Sann, A. Scott, Y. Shao, T. J. M. Symons, M. Tincknell, C. Tuvé, S. Wang, P. Warren, H. H. Wieman, T. Wienold, and K. Wolf, Phys. Rev. C **64**, 054602 (2001).
[37] J. Bondorf, A. Botvina, A. Iljinov, I. Mishustin, and K. Sneppen, Phys. Rep. **257**, 133 (1995).
[38] X. Campi, H. Krivine, E. Plagnol, and N. Sator, Phys. Rev. C **67**, 044610 (2003).
[39] E. Bonnet, D. Mercier, B. Borderie, F. Gulminelli, M. F. Rivet, B. Tamain, R. Bougault, A. Chbihi, R. Dayras, J. D. Frankland, E. Galichet, F. Gagnon-Moisan, D. Guinet, P. Lautesse, J. Łukasik, N. Le Neindre, M. Pârlog, E. Rosato, R. Roy, M. Vigilante, J. P. Wieleczko, and B. Zwieglinski (INDRA and ALADIN Collaborations), Phys. Rev. Lett. **103**, 072701 (2009).
[40] M. Pichon, B. Tamain, R. Bougault, F. Gulminelli, O. Lopez, E. Bonnet, B. Borderie, A. Chbihi, R. Dayras, J. Frankland, E. Galichet, D. Guinet, P. Lautesse, N. L. Neindre, M. Pârlog, M. Rivet, R. Roy, E. Rosato, E. Vient, M. Vigilante, C. Volant, J. Wieleczko, and B. Zwieglinski, Nucl. Phys. A **779**, 267 (2006).
[41] M. Begemann-Blaich, W. F. J. Müller, J. Aichelin, J. C. Adloff, P. Bouissou, J. Hubele, G. Imme, I. Iori, P. Kreutz, G. J. Kunde, S. Leray, V. Lindenstruth, Z. Liu, U. Lynen, R. J. Meijer, U. Milkau, A. Moroni, C. Ngô, C. A. Ogilvie, J. Pochodzalla, G. Raciti, G. Rudolf, H. Sann, A. Schüttauf, W. Seidel, L. Stuttge, W. Trautmann, and A. Tucholski, Phys. Rev. C **48**, 610 (1993).